Univerzita Karlova

Přírodovědecká fakulta

Studijní program: Chemie

Studijní obor: Chemie

Adam Alemayehu

Vývoj spirální magnetické struktury v kobalt chromitových nanočásticích

Size evolution of spiral magnetic structure in cobalt chromite nanoparticles

Bakalářská práce

Vedoucí práce: RNDr. Daniel Nižňanský, PhD.

Praha, 2017

Charles University

Faculty of Science

Study programme: Chemistry

Branch of study: Chemistry

Adam Alemayehu

Size evolution of spiral magnetic structure in cobalt chromite nanoparticles

Vývoj spirální magnetické struktury v kobalt chromitových nanočásticích

Bachelor´s thesis

Supervisor: RNDr. Daniel Nižňanský, PhD.

Prague, 2017

ČESTNÉ PROHLÁŠENÍ

Prohlašuji, že jsem bakalářskou práci zpracoval samostatně a že jsem uvedl všechny použité informační zdroje a literaturu. Tato práce ani její podstatná část nebyla předložena k získání jiného nebo stejného akademického titulu.

V Praze 9.5.2017

PODĚKOVÁNÍ

Touto cestou vyslovuji poděkování RNDr. Danielovi Nižňanskému, PhD. za pomoc, odborné vedení, cenné rady a připomínky při vypracování mé bakalářské práce. Zároveň děkuji M.Sc. Dominike Zákutné za odbornou konzultaci a za příležitost účastnit se výzkumu v Heinz Maier-Leibnitz Zentrum, Garching v Německu pod jejím vedením.

V Praze 9.5.2017

ABSTRAKT

Magnetické nanomateriály hrají důležitou roli v posledních desetiletích díky zajímavým aplikacím[1,2]. Multiferroické materiály jsou materiály, u nichž existují dva typy jevů, magnetické a feroelektrické uspořádání. To znamená, že se může indukovat magnetizace elektrickým polem nebo elektrická polarizace magnetickým polem. Oxid kobaltnato-chromitý patří do druhé skupiny multiferoických látek, nazývaných multiferroika typu II. Tyto multiferoické materiály jsou relativně nové. V případě, že v těchto materiálech existuje feroelektrika, musí být v těchto materiálech přítomen zvláštní typ magnetického uspořádání.

Oxid kobaltnato-chromitý ($CoCr_2O_4$) krystalizuje ve struktuře kubického spinelu, kde jsou Co^{2+} a Cr^{3+} umístěny v tetraedrických a oktaedrických polohách. Ve zhlucích dochází k ferrimagnetickému uspořádání $CoCr_2O_4$ při T_c = 94 K a systém dále prochází magnetickým fázovým přechodem na uspořádání do řady magnetických spirál s dlouhým dosahem při přechodové teplotě 26 K[3]. Současně byla pozorovaná dielektrická anomálie pod spirálním magnetickým přechodem. V této práci je prezentován vývoj spirálového uspořádání se změnou velikosti částic.

Klíčová slova: prášková röntgenová difrakce, difuzní rozptyl neutronů, hydrotermální metoda

ABSTRACT

Magnetic nanomaterials play an important role during the last decades due to interesting applications[1,2]. Multiferroic materials are materials where two types of phenomena coexist, magnetical and ferroelectrical ordering. It means that we can induce magnetization by an electric field or electrical polarization by a magnetic field. Cobalt chromite belongs to the second group of multiferroic materials, called Type-II multiferroics. These multiferroic materials are relatively new. The presence of ferroelectricity in these materials is due to special type of magnetic ordering.

Cobalt chromite ($CoCr_2O_4$) crystallizes in the cubic spinel structure, where Co^{2+} and Cr^{3+} are located on the tetrahedral and octahedral sites respectively. In the bulk system, the ferrimagnetic ordering of $CoCr_2O_4$ occurs at T_c = 94 K and undergoes an order-to-order magnetic phase transition to a long range spiral magnetic order at the transition temperature of 26 K[3]. At the same time, dielectric anomaly was observed below the spiral magnetic order. In our work we present the evolution of spiral ordering with changing of particle size.

Key words: powder X-ray diffraction, diffuse neutron scattering, hydrothermal method

CONTENTS

1 INTRODUCTION

Multiferroic materials, in particular those exhibiting magnetoelectric coupling, have recently attracted much attention since they are potentially of great use in electric devices such as dynamic random access memories, data storage media, telecommunication systems, electromagnetic sensors etc[4,5]. Cobalt-based catalysts, especially cobalt chromites, were found to be one of the best candidates for the catalytic combustion of methane[6,7]. As a typical multiferroic material, cobalt chromite ($CoCr_2O_4$) has shown to be unique, which not only displays uniform polarization and spatially modulated magnetism but also exhibits uniform magnetization in the conical cycloid state.[8]

Up to date, there are many studies of $CoCr_2O_4$ which were prepared by various synthesis approach as hydrothermal, template synthesis, sol gel method, microemulsion method[9] etc. The structural, magnetic, thermodynamic, and dielectric properties of polycrystalline $CoCr_2O_4$ were also investigated[10].

The $CoCr_2O_4$ nanoparticle were prepared using hydrothermal method. But after the synthesis amorphous phase was obtained and high temperature treatment was applied in order to obtain crystalline samples. The prepared samples were annealed at various temperatures from 300 - 550 ℃ with a particle size range of 3.1 - 15.2 nm.

In particular, the magnetic phase transition are well known in all form as polycrystalline, single crystal[11] and nanosized state. But there is a lack of direct establishing and in deep evaluation of spiral structure in nanosized $CoCr_2O_4$. In recent years also new studies were carried out about the microscopic magnetic structure of cobalt chromite nanoparticles and doped cobalt chromite nanoparticles, nevertheless authors claimed that the nanoparticles were of polycrystalline nature. In this contribution, the evolution of spiral magnetic structure will be discussed and presented. A detailed study of magnetic properties of nanosized $CoCr_2O_4$ were investigated on the microlevel by means neutron diffractions experiments with XYZ polarization analysis. This method give an opportunity to explain of spiral structure and it changes with temperature and size.

2 THEORETICAL PART

2.1 Basics of magnetism

Every electric and magnetic field is described by the four Maxwell equations:

$$\nabla \cdot \vec{D} = \varrho \quad \text{(Gauss` law)} \tag{2.1}$$

$$\nabla \times \vec{E} = -\frac{\partial \vec{B}}{\partial t} \quad \text{(Faraday`s law)} \tag{2.2}$$

$$\nabla \times \vec{H} = \vec{J} + \frac{\partial \vec{D}}{\partial t} \quad \text{(Ampère} - \text{Maxwell law)} \tag{2.3}$$

$$\nabla \cdot \vec{B} = 0 \quad \text{(Gauss` law for magnetism)} \tag{2.4}$$

where $\nabla \equiv \left(\frac{\partial}{\partial x}, \frac{\partial}{\partial y}, \frac{\partial}{\partial z}\right)$, $\vec{D}$ is the electric flux density, ϱ is the electric charge density, $\vec{E}$ is the intensity of the electric field, $\vec{B}$ is the magnetic flux density, $\vec{H}$ is the intensity of the magnetic field and $\vec{J}$ is the current density.

The magnetic properties of solids can be quantitatively described in terms of the magnetization $\vec{M}$ which is defined as the magnetic moment per unit volume.

$$\vec{M} = \frac{1}{V} \cdot \sum_{\mathrm{i}} \vec{\mu_{\mathrm{i}}} \tag{2.5}$$

where V is the volume of the substance and $\vec{\mu_{\mathrm{i}}}$ represents the magnetic moment of individual atoms.

The microscopic origin of magnetism is mostly the same in all magnets: it is the presence of localized electrons, mostly in the partially filled d or f shells of transition metals and rare-earth ions, which have a corresponding localised spin, or magnetic moment.

- Spin magnetic moment $\overrightarrow{\mu_s}$, which arises from the spin angular momentum of electron $\vec{S}$

$$\overrightarrow{\mu_s} = -\frac{g_0 \cdot \mu_B}{\hbar} \cdot \vec{S} \qquad (2.6)$$

where $g_0 \cong 2$ is the electron g-factor, $\mu_B \approx 9{,}274 \cdot 10^{-24}$ J T^{-1} is the Bohr magneton and $\hbar \approx 1{,}054 \cdot 10^{-34}$ J s is the reduced Planck constant.

- Orbital magnetic moment $\overrightarrow{\mu_l}$, which originate from orbital angular momentum of electron $\vec{L}$

$$\overrightarrow{\mu_l} = -\frac{\mu_B}{\hbar} \cdot \vec{L} \qquad (2.7)$$

- Induced magnetic moment, which originate from the change of orbital momentum induced by external field

Most solids are only weakly magnetic and develop a magnetization only when an external (vacuum) field is applied. In such cases, the amount of magnetization can be that is developed depends upon the magnitude of the magnetic susceptibility $\overleftrightarrow{\chi}$ which is defined by

$$\vec{M} = \overleftrightarrow{\chi} \cdot \vec{H} \qquad (2.8)$$

where $\vec{H}$ is the applied external field and $\overleftrightarrow{\chi}$ is in general a tensor in a crystalline solid.

Materials for which $\chi < 0$ are denoted as diamagnetic and the induced magnetization has an opposite direction as the applied magnetic field. Materials for which $\chi > 0$ are paramagnetic[12]. These materials do not exhibit spontaneous magnetization.

Materials which exhibit a magnetization $\vec{M}$ without application of an external field typically have much larger values for χ and can be ferromagnetic, antiferromagnetic or ferrimagnetic. Some types of these magnetic structures are given in **Figure 2.1**.

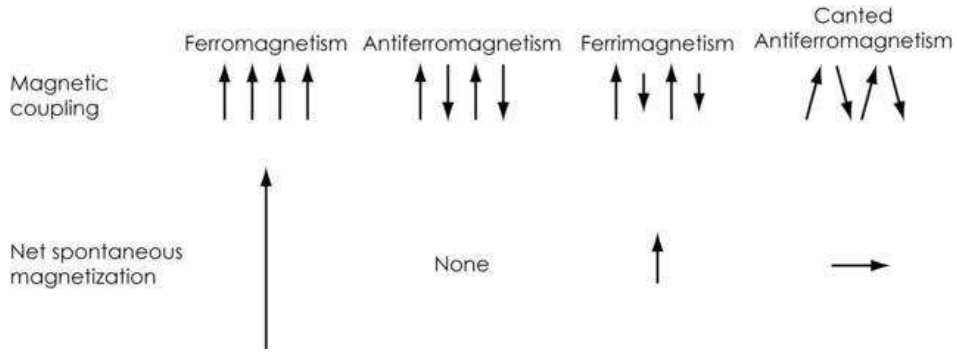

Figure 2.1: Some types of magnetism[13].

The magnetic flux density (magnetic induction) $\vec{B}$ inside a material is related to the magnetic field strength $\vec{H}$ through permeability $\overleftrightarrow{\mu}$

$$\vec{B} = \mu_0(\vec{H} + \vec{M}) = \mu_0(\vec{H} + \overleftrightarrow{\chi} \cdot \vec{H}) = \mu_0(\overleftrightarrow{1} + \overleftrightarrow{\chi})\vec{H} = \mu_0\overleftrightarrow{\mu_r} \cdot \vec{H} = \overleftrightarrow{\mu} \cdot \vec{H} \qquad (2.9)$$

$$\overleftrightarrow{\mu} = \mu_0(\overleftrightarrow{1} + \overleftrightarrow{\chi}) \qquad (2.10)$$

where $\overleftrightarrow{1}$ is the unit second rank tensor, $\mu_0 = 4\pi \cdot 10^{-7}$ H m^{-1} is the permeability of free space and $\overleftrightarrow{\mu_r}$ is the relative permeability tensor.

The Hamiltonian of an atom in a magnetic field changes[14]:

- The kinetic energy of each electron is changed $\vec{p} \to \vec{p} + e \cdot \vec{A}$, where $\vec{p}$ is the momentum of the electron without an external field, $e = 1.602 \cdot 10^{-19}$ C is the elementary charge and $\vec{A}$ is the vector potential defined as

$$\vec{B} = \nabla \times \vec{A} \tag{2.11}$$

$$\nabla \cdot \vec{A} = 0 \tag{2.12}$$

  Usually take $\vec{A}$ to be $\vec{A} = -\frac{1}{2} \cdot \vec{r} \times \vec{B}$.

  The kinetic energy of the nucleus is unchanged due to large mass.

- The interaction energy of electron spin with the external field is added to the Hamiltonian[14]:

$$\mathcal{H} = \frac{g_0 \cdot \mu_B}{\hbar} \cdot \vec{S} \cdot \vec{B} \tag{2.13}$$

The total kinetic energy is now[14]:

$$T = T_0 + \frac{\mu_B}{\hbar} \cdot \vec{L} \cdot \vec{B} + \frac{e^2}{8 \cdot m} \cdot B^2 \cdot \sum_i (x_i^2 + y_i^2) \tag{2.14}$$

where $m = 9{,}1 \cdot 10^{-31}$ kg is the mass of the electron.

Adding the spin interaction energy to this gives[14]:

$$\Delta\mathcal{H} = \frac{\mu_B}{\hbar} \cdot \left(\vec{L} + g_0 \cdot \vec{S}\right) \cdot \vec{B} + \frac{e^2}{8m} \cdot B^2 \cdot \sum_i (x_i^2 + y_i^2) \tag{2.15}$$

Using second order perturbation theory to get values of the energy change ΔE_n due to the magnetic field gives[14]:

$$\Delta E_n = \frac{\mu_B}{\hbar}\vec{B}\langle n|\vec{L} + g_0\vec{S}|n\rangle + \sum_{n\neq n`} \frac{\left|\left\langle n\left|\frac{\mu_B}{\hbar}(\vec{L} + g_0\vec{S})\vec{B}\right|n`\right\rangle\right|^2}{E_n - E_{n`}} + \frac{e^2B^2}{8m}\langle n|\sum_i(x_i^2 + y_i^2)|n\rangle \qquad (2.16)$$

From this energy expression we can get the magnetic susceptibility of individual atoms, ions and molecules.

2.2 Multiferroic materials

Multiferroic materials (multiferroics) are materials in which two types of ordering exist in the absence of external electric and magnetic fields: ferromagnetism, the spontaneous ordering of orbital and spin magnetic moments, and ferroelectricity, the spontaneous ordering of electric dipole moments[15]. In principle a third type of ordering, spontaneous deformation, which leads to ferroelasticity is often included[16].

In general there are two groups of multiferroics:

- Those in which ferroelectricity and magnetism have different sources and appear largely independently of one another, though there is some coupling between them. These multiferroics are called type-I multiferroics and ferroelectricity typically appears at higher temperatures than magnetism[16].

- The second group is called type-II multiferroics. Here, magnetism causes ferroelectricity, implying a strong coupling between them. The polarization in these materials is usually much smaller[16].

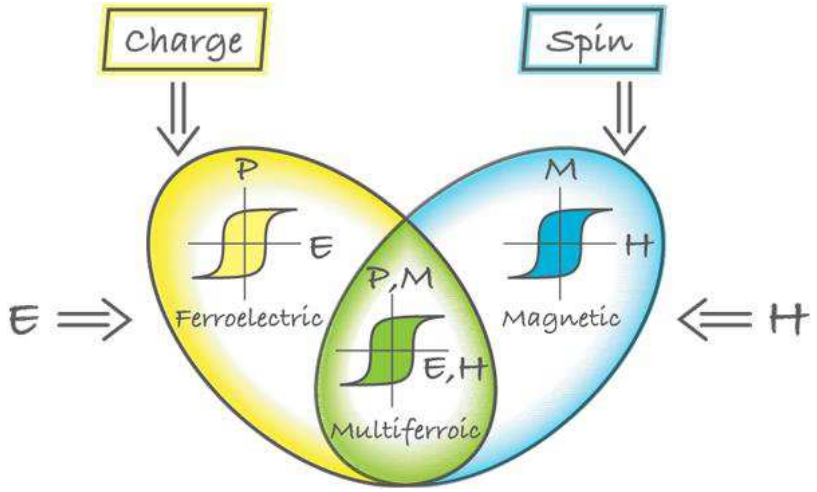

Figure 2.2: Ilustration of orderings in magnetoelectric and multiferroic materials[16].

2.2.1 Type-I multiferroics

Type-I multiferroics are known for longer time and more numerous. They are good ferroelectrics and the critical temperature of the magnetic and ferroelectric transitions are often well above room temperature. The coupling between magnetism and ferroelectricity in these materials is weak. Type-I multiferroics have several different subclasses, depending on the mechanism of ferroelectricity in them[16].

The most known ferroelectrics are the perovskites ($ATiO_3$)[16]. Ferroelectricity in these systems is caused by the off-center shifts of the transition metal ions, which forms strong covalent bonds with one or three oxygens, using their empty d-orbitals.

Bi^{3+} and Pb^{2+} also play the major role in the origin of ferroelectricity. The two outer 6s electrons that do not participate in chemical bonds. These lone pairs have large polarizability, which is required for ferroelectricity of classical type[16].

Charge ordering also causes ferroelectricity, observed in transition metal compounds. Especially those containing transition metal ions with different valence.

2.2.2 Type-II multiferroics

In these materials ferroelectricity exists only in a magnetically ordered state and is caused by particular type of magnetism[16]. Type-II multiferroics are divided into two groups:

- Ferroelectricity is caused by particular type of magnetic spiral structure
- Ferroelectricity appears also for collinear magnetic structures

2.2.2.1 Spiral multiferroics

Most of the type-II multiferroics belong to this group. When the spins form a spiralling magnetic phase (cycloidal) along a specific crystallographic direction, every nearest spin-pair produces the unidirectional local $\vec{P}$ and so the macroscopic polarization of magnetic origin is observed[17]. The spontaneous polarizations is then:

$$\vec{P} = a \cdot \sum_{ij} \overrightarrow{e_{ij}} \times \left(\overrightarrow{S_i} \times \overrightarrow{S_j}\right) \qquad (2.17)$$

where a is a proportional constant determined by spin-orbit and spin exchange interactions, $\overrightarrow{e_{ij}}$ is the unit vector connecting the neighbouring spins $\overrightarrow{S_i}$ and $\overrightarrow{S_j}$. Spin helicity is the clockwise or counterclockwise rotation of the spin and it determines the positive or negative sign of the polarization[17].

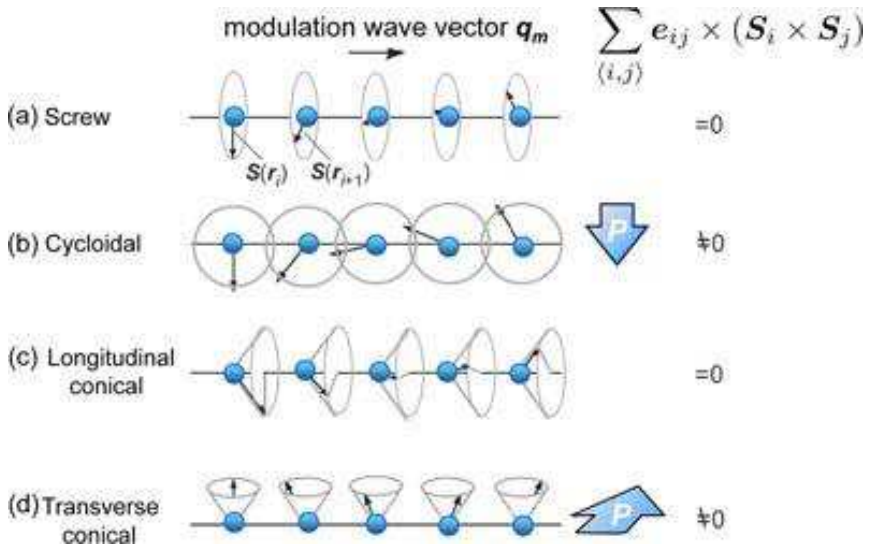

Figure 2.3: Illustration of spiral magnetic structures[17].

Induced polarization can also emerge from spin waves (magnons). Here all spins are oriented in one direction, but the size of the local moments varies periodically in space, **Figure 2.3**.

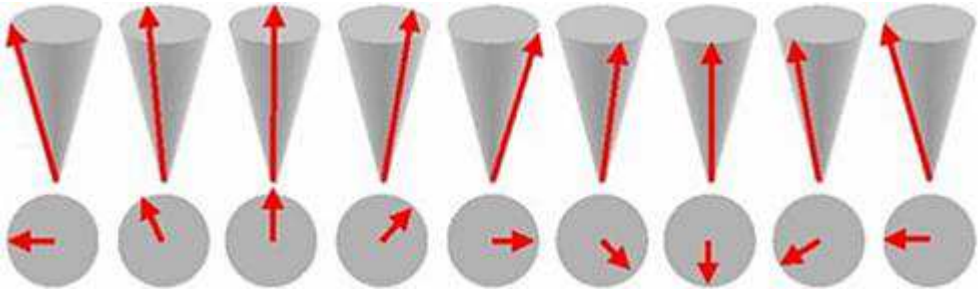

Figure 2.4: Spin wave (one complete precession distributed over a chain of spins)[18].

2.3 Characterization methods

2.3.1 Neutron scattering

Neutron scattering is one of the most useful and versatile experimental methods to study the structure and dynamics of matter on the atomic and nanometer scale[19]. Neutrons have no charge and their electric dipole moment is either zero or too small to be measured by the most sensitive modern techniques. Due to this fact neutrons can penetrate matter much better than charged particles. In addition, neutrons interact with matter through nuclear forces which are very short range. Neutrons can penetrate given matter a long distance without being absorbed or scattered, **Figure 2.5**.

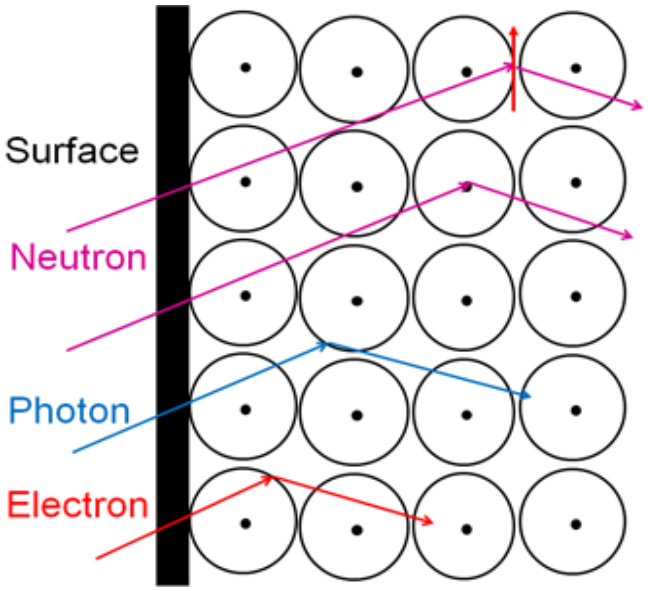

Figure 2.5: Beams of neutrons, photons and electrons interact with matter by different mechanism. Electrons (red) and photons (blue) interact with matter by electrostatic and electromagnetic interactions respectively. Neutrons (purple) interact with matter via strong nuclear forces (purple bottom). The interaction can be a dipole-dipole interaction (purple top) with unpaired electrons[20].

2.3.1.1 Basics of neutron scattering

The flux of a neutron beam is defined as the neutron rate per area:

$$\phi = \frac{nuber\ of\ neutrons\ impinging\ on\ a\ surface\ per\ second}{surface\ area\ perpendicular\ to\ the\ neutron\ beam\ direction} \quad (2.18)$$

The neutron scattering cross section, σ, of a system is defined by its ability to scatter neutrons[19]:

$$\sigma = \frac{1}{\phi} \cdot N \quad (2.19)$$

where N is the number of neutrons scattered per second.

The scattering cross section is dependent on the scattered angle. The angular dependence of the scattered neutrons is described by differential scattering cross section:

$$\frac{d\sigma}{d\Omega} = \frac{1}{\phi} \cdot \frac{dN}{d\Omega} \quad (2.20)$$

where dN is the number of neutrons scattered into solid angle $d\Omega$ per second.

In some scattering processes, the neutrons deliver energy to or absorb energy from the scattering system. This type of scattering is described as inelastic scattering. The neutron energy transfer is defined as[19]:

$$\hbar \cdot \omega = E_f - E_i = \frac{\hbar^2 \cdot \left(k_f^2 - k_i^2\right)}{2 \cdot m} \quad (2.21)$$

where i and f represent the initial and final state respectively, k is the wave vector, ω is the angular frequency and m is the rest mass of the neutron.

For describing inelastic scattering we need to take into account the energy dependence of the scattered neutrons. The partial differential cross section is defined as[19]:

$$\frac{d^2\sigma}{d\Omega dE_f} = \frac{1}{\phi} \cdot \frac{d^2N}{d\Omega dE_f} \quad (2.22)$$

where d^2N is the number of neutrons scattered into a solid angle $d\Omega$ per second with energies $\left[E_f; E_f + dE_f\right]$.

2.3.1.2 Quantum mechanics of scattering

We define the state of the incoming wave as[19]:

$$|\psi_i\rangle = \frac{1}{\sqrt{V}} \cdot e^{i \cdot \vec{k_i} \cdot \vec{r}} \tag{2.23}$$

where, $V = L^3$, is the normalization volume for a state enclosed in a cubic box in a cubic box with side length L. The incoming neutron flux is then[19]:

$$\phi_i = |\psi_i|^2 \cdot v = \frac{1}{V} \cdot \frac{\hbar \cdot k_i}{m} \tag{2.24}$$

The final state can be expressed as a wave:

$$|\psi_f\rangle = \frac{1}{\sqrt{V}} \cdot e^{i \cdot \vec{k_f} \cdot \vec{r}} \tag{2.25}$$

The energy density for a wave function emitted into directions of $\vec{k_f}$, corresponding to solid angle $d\Omega$ in k-space is[19]:

$$\left(\frac{dn}{dE_f}\right)_{d\Omega} = \frac{V \cdot k_f \cdot m}{(2\pi)^3 \cdot \hbar^2} d\Omega \tag{2.26}$$

The scattering process itself is described by the Fermi golden rule. The number of neutrons scattered into $d\Omega$ per second, dN, is then given as:

$$dN = \frac{V \cdot k_f \cdot m}{(2\pi)^2 \cdot \hbar^3} d\Omega \cdot \left|\langle \psi_f | \hat{V} | \psi_i \rangle\right|^2 \tag{2.27}$$

Using equation (2.42), (2.39) and (2.35) the differential scattering cross section is then:

$$\frac{d\sigma}{d\Omega} = V^2 \cdot \frac{k_f}{k_i} \cdot \left(\frac{m}{2\pi \cdot \hbar^2}\right)^2 \cdot \left|\langle \psi_f | \hat{V} | \psi_i \rangle\right|^2 \qquad (2.28)$$

The interaction between the neutron and the nucleus is expressed by the Fermi pseudopotential[19]:

$$\hat{V}_j(\vec{r}) = \frac{2\pi \cdot \hbar^2}{m} \cdot b_j \cdot \delta\left(\vec{r} - \vec{r_j}\right) \qquad (2.29)$$

where b_j is the scattering length and $\vec{r_j}$ is the position of the nucleus.

The differential scattering cross section for one nucleus can be shown that is equal to:

$$\frac{d\sigma}{d\Omega} = {b_j}^2 \qquad (2.30)$$

2.3.1.3 Coherent and incoherent scattering

The scattering length, b, varies randomly from nucleus to nucleus in a sample. b is different for different isotopes of a given element and also for different nuclear spin states. This gives rise to an additional contribution to the total intensity, the incoherent scattering[21], **Figure 2.6**.

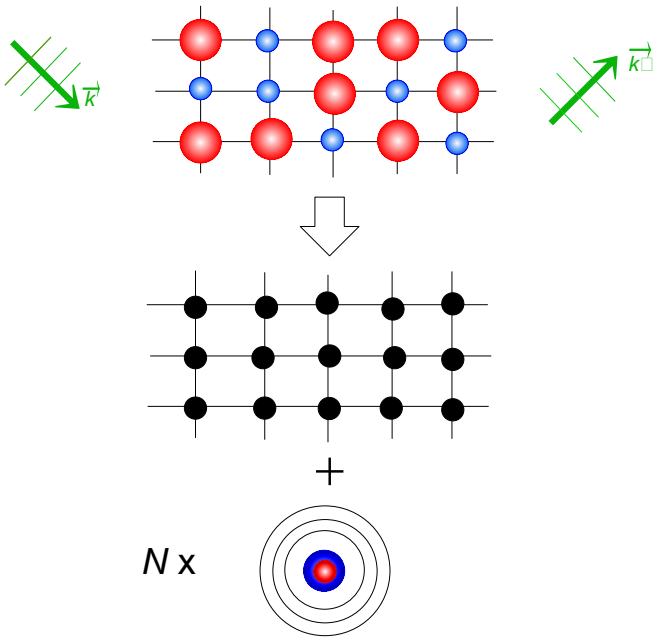

Figure 2.6: Upper panel: Diffraction from a 2D crystal with two isotopes of the same element with two scattering lengths b_i and b_j. Middle panel: coherent scattering from the mean gives rise to Bragg peaks, Lower panel: an isotropic background is observed and is proportional to the number of atoms N[21].

For calculating the scattering cross section a random distribution of different isotopes in the sample must be considered. Therefore, we have to average over the random distribution of the scattering length in the sample[21].

$$\frac{d\sigma}{d\Omega} = \langle b \rangle^2 \cdot \left| \sum_i e^{i\vec{Q}\cdot\vec{r_i}} \right|^2 + N \cdot \langle (b - \langle b \rangle)^2 \rangle \qquad (2.31)$$

$$\vec{Q} = \overrightarrow{k_f} - \overrightarrow{k_i} \qquad (2.32)$$

where $\vec{Q}$ is the scattering vector.

The first term in (2.31) contains a phase factors, $e^{i\vec{Q}\cdot\vec{r_i}}$ and gives an information on an average of b[21]. It also takes into account interference effects and is called coherent scattering. There are two types of coherent scattering, one with and without the conservation of energy know as elastic and inelastic scattering, respectively. Elastic coherent scattering gives an information on the structure of material and inelastic coherent scattering arises from the collective motion as for example phonons. The second term does not contain phase information and is proportional to the number of atoms, N which determine the deviation from an average of b and is called incoherent scattering. The incoherent scattering can also be elastic (isotropic scattering) and inelastic (atomic diffusion, phonon density).

2.3.1.4 Spin dependent interactions

Consider a nucleus with nuclear spin $I \neq 0$. The spin of the neutron and nucleus can be randomly oriented. The spin state, J, during the scattering process can have two possible values: $J_+ = I + \frac{1}{2}$ and $J_- = I - \frac{1}{2}$. J_+ stands for the spin state when the spin of the neutron and nucleus are parallel and J_- stands for the spin state when the spin of the neutron and nucleus are antiparallel[21]. The multiplicity of the spin state is $2J + 1$ and thus the

multiplicities are $2I+2$ and $2I$ for J_+ and J_- respectively. The total number of configurations is then $4I+2$.

The probabilities (for unpolarised neutrons) p_+ and p_- for realizing state J_+ and J_- respectively are[21]:

$$p_+ = \frac{I+1}{2I+1} \qquad p_- = \frac{I}{2I+1} \tag{2.33}$$

For all isotopes with nuclei that have $I \neq 0$, the scattering lengths b_+ and b_- are different. This gives rise to spin incoherent scattering.

The spin incoherent differential cross section is then[21]:

$$\left(\frac{d\sigma}{d\Omega}\right)_{\text{spin inco}} = N \cdot \frac{I(I+1)(b_+ - b_-)^2}{(2I+1)^2} = N \cdot B^2 \cdot I(I+1) = N \cdot {b_{inc}}^2 \tag{2.34}$$

where $B = \frac{b_+ - b_-}{2I+1}$ and $b_{inc} = B \cdot \sqrt{I(I+1)}$ is the spin incoherent scattering length.

2.3.1.5 Magnetic interactions

Neutrons have nonzero magnetic dipole moment and thus can interact with magnetic field and thus also with the magnetic dipolar moment originating from unpaired electronic spins. The dipolar interaction potential, V_M, of neutron magnetic moment, $\vec{\mu}$, with magnetic field, $\vec{B}$, is:

$$V_M = -\vec{\mu} \cdot \vec{B} \tag{2.35}$$

The gyromagnetic ratio of the neutron, γ, is[21]:

$$\gamma = \frac{2 \cdot \gamma_N \cdot \mu_N}{\hbar} \approx -1.83 \cdot 10^8 \ \mathrm{s^{-1}\,T^{-1}} \tag{2.36}$$

where γ_N is the gyromagnetic factor of the neutron and $\mu_N \approx 5{,}05 \cdot 10^{-27}\ \mathrm{J\,T^{-1}}$ is the nuclear magneton.

The magnetic field created by the electronic spin at position $\vec{r}$ is (Biot-Savart law) [21]:

$$\overrightarrow{B_s} = -2\mu_B \cdot \nabla \times \left(\frac{\hat{s} \times \vec{r}}{r^3}\right) \tag{2.37}$$

And the magnetic field created by orbital motion of the electron at position $\vec{r}$ is[21]:

$$\overrightarrow{B_l} = -\frac{e}{c} \cdot \frac{\overrightarrow{v_e} \times \vec{r}}{r^3} \tag{2.38}$$

The scattering potential is then:

$$V_M = -\vec{\mu} \cdot \left(\overrightarrow{B_s} + \overrightarrow{B_l}\right) = \vec{\mu} \cdot \left[2\mu_B \cdot \nabla \times \left(\frac{\hat{s} \times \vec{r}}{r^3}\right) + \frac{e}{c} \cdot \frac{\overrightarrow{v_e} \times \vec{r}}{r^3}\right] \tag{2.39}$$

The differential scattering cross section is[21]:

$$\left(\frac{d\sigma}{d\Omega}\right)_{\text{mag}} = (\gamma_N \cdot r_0)^2 \cdot \left|\frac{1}{2\mu_B} \cdot \left\langle S_z^{`} \middle| \hat{\sigma} \cdot \overrightarrow{M_\perp}(\vec{Q}) \middle| S_z \right\rangle\right|^2 \tag{2.40}$$

where r_0 is the classical radius of the electron, $\hat{\sigma}$ is the vector spin operator and $\overrightarrow{M_\perp}(\vec{Q})$ is the magnetization perpendicular to the scattering vector $\vec{Q}$. Only the component of the magnetization perpendicular to the scattering vector contributes to the scattering cross section[21], **Figure 2.7**.

The geometrical condition of magnetization and scattering vector are given by Harper-Johnson vector (obtained as Fourier transformation of vector from real space) [21]:

$$\overrightarrow{M_\perp} = \hat{Q}\text{x}(\vec{M}\text{x}\hat{Q})$$

where $\hat{Q}$ is a unitary scattering vector.

By the applying magnetic field in certain direction (perpendicular/parallel to the scattering vector) give us an opportunity to separate scattering contributions with using of polarized neutrons.

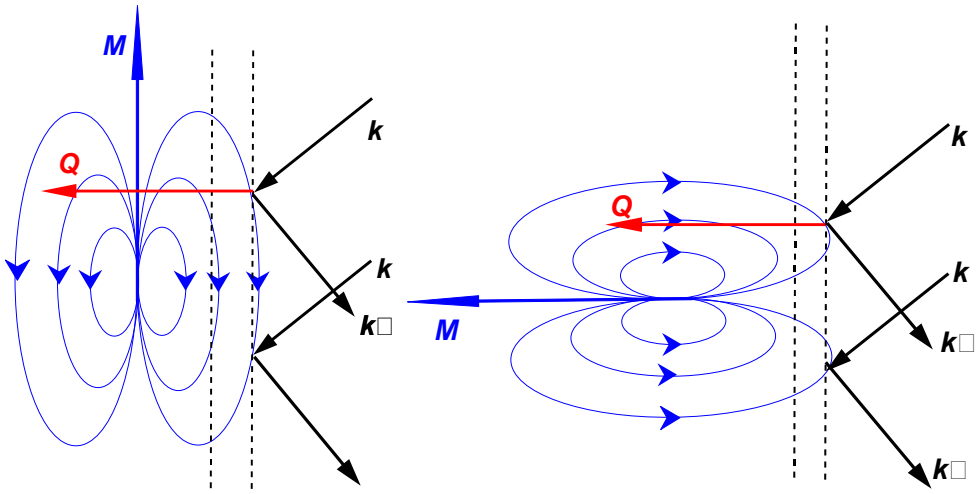

Figure 2.7: The magnetic field line configuration for magnetic scattering of a neutron[21].

2.3.1.6 Diffuse neutron spectroscopy

DNS is a versatile diffuse scattering cold neutron time-of-flight spectrometer with polarization analysis[22] (**Figure 2.8.**). It can work as neutron diffractometer or in TOF mode (using the set of choppers) in order to study atomic and magnetic diffuse scattering. Velocity selector is used to obtain quasi-monochromatic neutron beam of certain wavelength. The neutrons are polarized by supermirrors and on the sample position is xyz-coils which allow to apply very small magnetic field in order to change polarization of neutron in certain direction (x,y,z) at sample.

For the single crystals, the separation rules are given by (only for magnetic part) [21]:

$$\begin{pmatrix} \Gamma^{x}_{\uparrow\downarrow}(\vec{r},\omega) \\ \Gamma^{y}_{\uparrow\downarrow}(\vec{r},\omega) \\ \Gamma^{z}_{\uparrow\downarrow}(\vec{r},\omega) \\ \Gamma^{x}_{\uparrow\uparrow}(\vec{r},\omega) \\ \Gamma^{y}_{\uparrow\uparrow}(\vec{r},\omega) \\ \Gamma^{z}_{\uparrow\uparrow}(\vec{r},\omega) \end{pmatrix} = \begin{pmatrix} \sin^2\alpha\cos^2\alpha & \cos^4\alpha & 1 & -\sin\alpha\cos^3\alpha \\ \sin^4\alpha & \sin^2\alpha\cos^2\alpha & 1 & -\sin^3\alpha\cos\alpha \\ \sin^2\alpha & \cos^2\alpha & 0 & -\sin\alpha\cos\alpha \\ \sin^4\alpha & \sin^2\alpha\cos^2\alpha & 0 & -\sin^3\alpha\cos\alpha \\ \sin^2\alpha\cos^2\alpha & \cos^4\alpha & 0 & -\sin\alpha\cos^3\alpha \\ 0 & 0 & 1 & 0 \end{pmatrix} = \begin{pmatrix} M_{xx}(\vec{r},\omega) \\ M_{yy}(\vec{r},\omega) \\ M_{zz}(\vec{r},\omega) \\ M_{xy}(\vec{r},\omega) + M_{yx}(\vec{r},\omega) \end{pmatrix} \tag{2.41}$$

where $\Gamma^{x}_{\uparrow\downarrow}$ is representing function with polarization applied in *x* direction and for spin flip (for non-spin flip scattering the notation is ↑↑), M_{xx}, M_{yy}, M_{zz}, M_{xy}, M_{yx}, corresponds to the components of the magnetization in certain direction.

This separation rules become simple when sample is in paramagnetic state (where cross magnetization components can be neglected and $\langle M_x^2\rangle = \langle M_y^2\rangle = \langle M_z^2\rangle$) and for isotropic distribution of magnetization as it is in case of powder.

Therefore, DNS allows unambiguous separations of nuclear coherent, spin incoherent and magnetic scattering contributions over a large range of scattering vector Q and energy transfer E by *xyz* polarization analysis[21]:

$$\sigma_{coh} = \sigma_z^{SF} - \frac{1}{2}\sigma_{para} - \frac{1}{3}\sigma_{incoh} \tag{2.42}$$

$$\sigma_{\text{incoh}} = \frac{3}{2}\left(3\sigma_{\text{z}}^{\text{SF}} - \sigma_{\text{x}}^{\text{SF}} - \sigma_{\text{y}}^{\text{SF}}\right) \tag{2.43}$$

$$\sigma_{mag} = 2\left(\sigma_x^{SF} + \sigma_y^{SF} - 2\sigma_z^{SF}\right) = -2\left(\sigma_x^{NSF} + \sigma_y^{NSF} - 2\sigma_z^{NSF}\right) \tag{2.44}$$

where SF and NSF corresponds to spin flip and non-spin flip scattering, respectively and the *x, y, z* are the direction of the polarization on the sample.

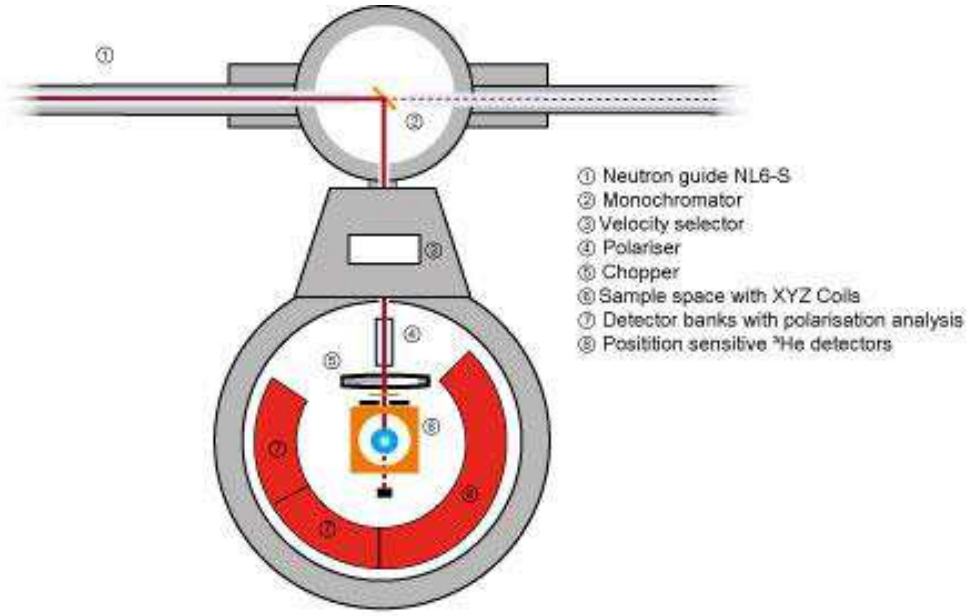

Figure 2.8: Scheme of DNS instrument[22].

2.4 Structure of $CoCr_2O_4$

Spinel is a mineral with formula $MgAl_2O_4$. The spinel minerals have a generic formula of AB_2O_4, where A stands for a cation with +2 charge and B stands for a cation with +3 charge. Oxygens in spinel form a face-centered cubic (fcc) lattice. The cubic spinel structure is characterized by space group $Fd\bar{3}m$. Each unit cell contains 8 formula units AB_2O_4, thus there are 32 oxygen ions in a unit cell[23].

In the normal spinel structure the A cations fill 1/8 of the tetrahedral sites and the B cations fill 1/2 of the octahedral sites.

Inverse spinel□s unit cell has the same size. In this unit cell the A ions and half of the B ions switch sites and thus inverse spinels are formulated as $B(AB)O_4$, where the (AB) ions occupy the octahedral sites[23].

Transition metal oxides form spinel and inverse spinel structures. The choice between them is driven by the crystal field stabilization energy of ions in the tetrahedral and octahedral sites. For 3d elements the configuration is typically high spin because O^{2-} are weak field ligand[24].

$CoCr_2O_4$ is a spinel ferrimagnet, where Co^{2+} cations are located in A sites and Cr^{3+} are located in B sites, **Figure 2.9**. $CoCr_2O_4$ is a normal spinel, as well as every other chromite, because the Cr^{3+} (d^3) ion has a strong preference for the octahedral sites[24].

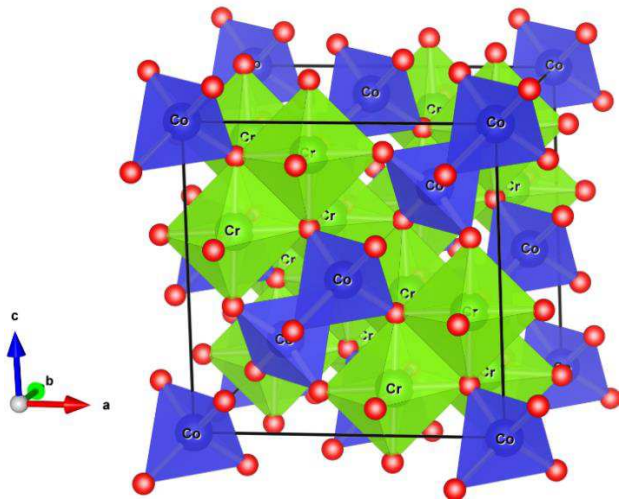

Figure 2.9: Crystal structure of $CoCr_2O_4$[25].

2.5 Hydrothermal method

Hydrothermal reaction is any heterogeneous reaction in a presence of a solvent (whether aqueous or non-aqueous) above room temperature at pressure greater than 1 atm in a closed system[26]. It is a general method for preparing inorganic salts and for crystal growth. Hydrothermal synthesis also enables to prepare compounds with an unusual oxidation state such as chromium (IV) oxide[27]. The most frequently used medium in hydrothermal synthesis is water. One of the biggest advantages of using water is the environmental benefit and cheaper than other solvents, and it can act as a catalyst for the formation of desired materials by tuning temperature and pressure[28]. Various mineralizers are also added to water. Mineralizers are complexing agents that act to increase the solubility of the starting precursors by forming soluble complexes[29]. The whole synthesis is carried out in autoclaves, where various metal salts react with fatty acids, alcohol and wader and are treated at increased temperature. This preparation leads to nanoparticles caped with fatty acids.

3 EXPERIMENTAL PART

In this part I will focus on the preparation of isolated nanoparticles of cobalt chromite and their characterization.

3.1 Chemicals

ethanol absolute	Penta-chemicals, p.a.
hexane	Lach-ner
oleic acid	Aldrich, tech. 90%
sodium hydroxide	Lach-ner, p.a., micropearls
cobalt (II) chloride hexahydrate	Penta-chemicals, p.a.
chromium (III) chloride hexahydrate	Aldrich, ≥98%

3.2 Synthesis of nanoparticles of $CoCr_2O_4$

The analysed samples were prepared by hydrothermal method in autoclave with 50ml teflon liner. The solution of metal chlorides was prepared by dissolving chromium and cobalt chloride hexahydrate in molar ratio (Cr^{3+}: Co^{2+}= 2:1). This solution was mixed with the solution of sodium oleate, which was prepared mixing 10 mmol (400 mg) of sodium hydroxide in a small amount of water and ethanol solution with 12 mmol (3,39 g) of oleic acid**.** The water solution of the metal ions and the oleate solution was mixed and the mixture was sonicated for 5 minutes. The final two phase solution was put into the autoclave and placed into the oven for 16 hours at 200 °C.

After cooling down the liquid phases were discarded and the sedimented nanoparticles were dispersed in 15 ml of hexane. The non-dispersed nanoparticles (aggregates) were separated by centrifugation (5 min, 3500 rpm) and the hexane phase was used for the following preparation. The nanoparticles were precipitated with 10 ml of ethanol. The precipitated nanoparticles were separated by centrifugation. This procedure was repeated 3 times.

The prepared amorphous phase was then annealed at 250 °C, 300 °C, 350 °C, 400 °C, 450 °C, 500 °C and at 550 °C for 2 hours.

3.3 Characterization methods

- The XRD patterns were recorded from 5 to 80° (2θ) on PANalytical X`Pert PRO using CuK_{α}. The diffraction pattern was recorded in step scan mode with step width of 0,02°.

- Transmission Electron Microscopy (TEM) was carried out using a ZEISS LEO 902 operating at 120 kV with LaB6 cathode in bright field (BF) mode. The sample was deposited onto a coated copper grid, the mean particle diameter was statistically determined from at least 200 particles in different BF images and fitted with the log-normal distribution function using the imageJ software[30].

- Polarized neutron scattering experiments of cobalt chromite samples with particle diameter in the range of 3.1 to 15.2 nm were measured at various temperatures from 3.2 K to 100 K on DNS instrument using the neutron wavelength of 4.2 Å. The reference measurement of a NiCr alloy yields the flipping ratio correction and thus the real polarization of the incident neutron beam. Vanadium was measured for calibration of the detector efficiency. The magnetic, nuclear coherent and spin–incoherent contribution were separated from the total scattering by means of xyz-polarization method. The measurements were carried out at Heinz Maier-Leibnitz Zentrum, Garching, Germany.

4 RESULTS AND DISCUSSION

4.1 Powder X-ray Diffraction

The phase composition of the prepared samples was determined by powder X-ray diffraction. The X-ray diffraction patterns of all prepared samples show the presence of spinel structure with space group of $Fd\bar{3}m$ (**Figure 4.1**). Also each sample is containing Bragg's maxima of NaCl, which can be caused by inefficient washing of the samples after the hydrothermal preparation. This phase is diamagnetic and does not impair magnetic behaviour. The phase analysis was carried out using search-match function of PANalytical X'Pert PRO for CuK_α radiation. The diffraction patterns also show that the particle size is increasing with the increasing annealing temperature. Which can be followed by change of the full with of half maxima of the peaks as it is described by Scherrer equation[31]:

$$d = \frac{K \cdot \lambda}{B \cdot \cos\theta} \qquad (4.1)$$

where K is Scherer's constant, λ is the wavelength of the used x-ray radiation and B is the width of diffracted peak (in angle θ).

From **Figure 4.2**. we can see the temperature change of particle size obtained by using Scherrer equation. The particle sizes, obtained from Sherrer equation, show an increasing trend on the annealing temperature. This trend is also proved with the particle sizes obtained from TEM analysis, **Figure 4.4**.

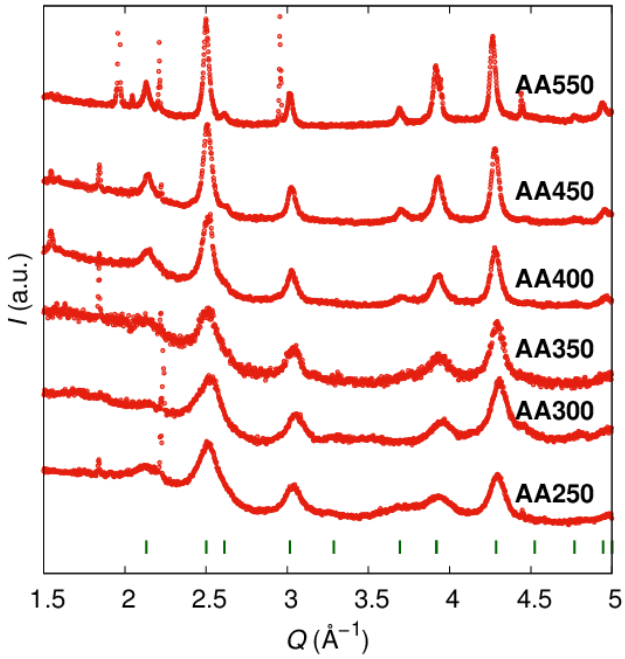

Figure 4.1: Powder X-ray diffraction patterns of the samples. The green vertical lines correspond to Bragg□s maxima of $CoCr_2O_4$.

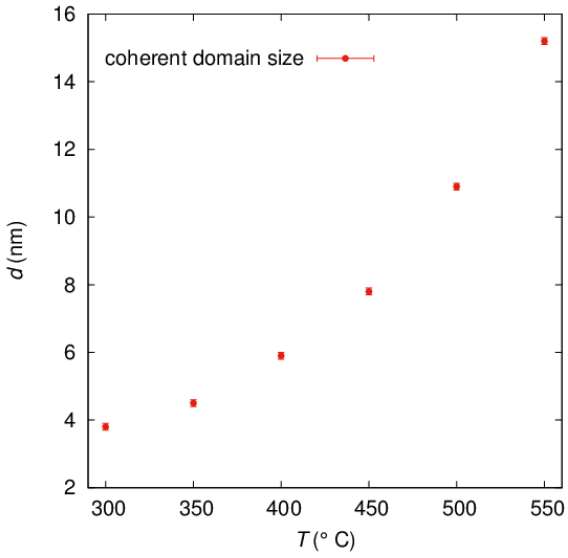

Figure 4.2: Dependence of the particle size obtained from Sherrer equation on the annealing temperature.

4.2 Transmission electron microscopy

The morphology of the nanoparticles was analysed by TEM in bright field mode. TEM micrographs (**Figure 4.3**) reveals nearly spherical morphology of nanoparticles. Also, it can be seen from micrographs that individuals nanoparticles are present in the sample without aggregation to bigger sizes caused by annealing procedure. The distribution of particle sizes are presented in **Figure 4.4**. The particle sizes obtained from TEM analysis are bigger than the ones obtained from the PXRD patterns using the Sherrer equation (**Figure 4.5**). The difference between them is caused by the fact that the size of the domain which can scatter X-rays and hence can be seen by the PXRD method is smaller than the whole particle which is seen by the TEM analysis.

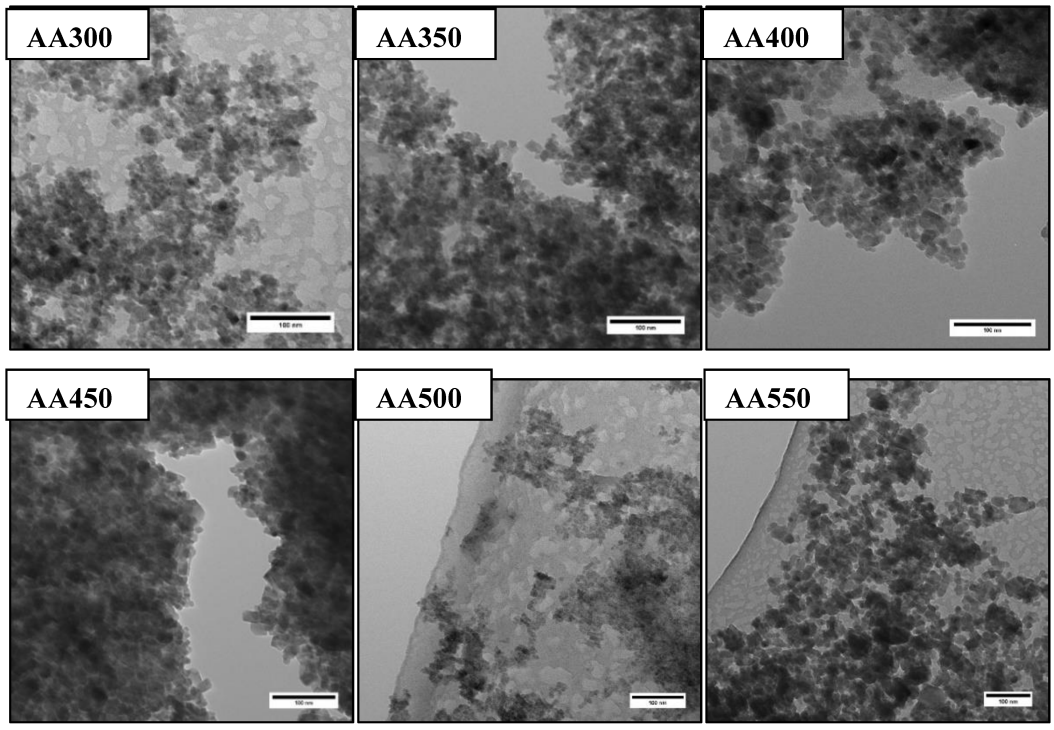

Figure 4.3: TEM micrographs of prepared samples. (Scale bars: 100 nm)

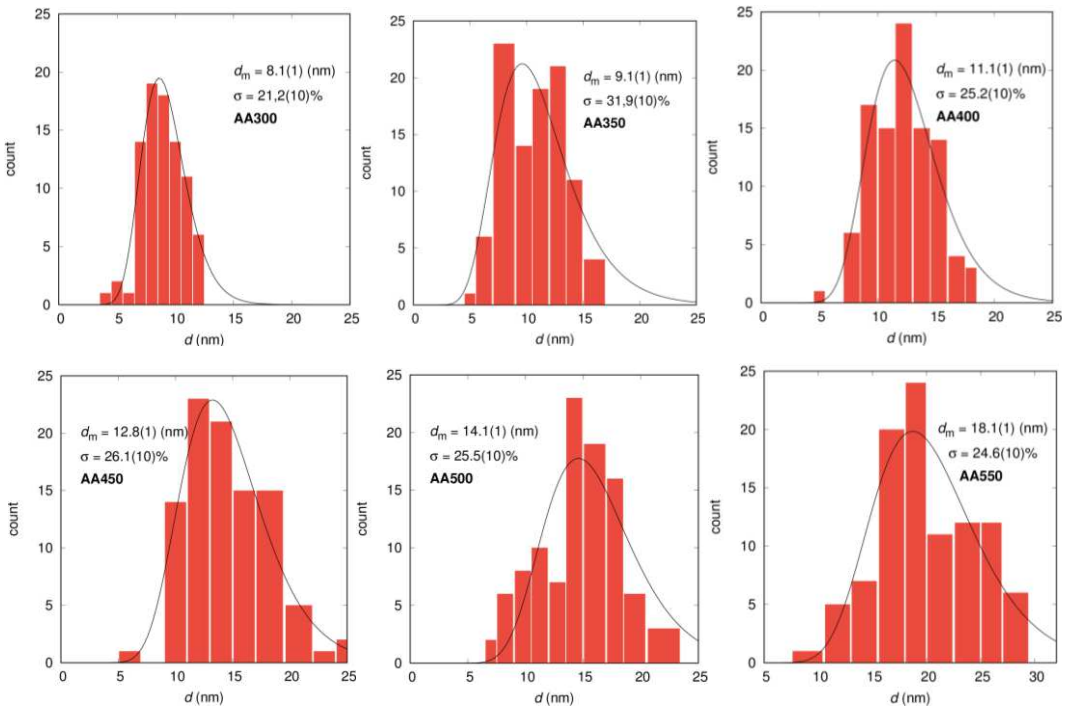

Figure 4.4: LogNormal size distribution of prepared samples obtained from TEM micrographs.

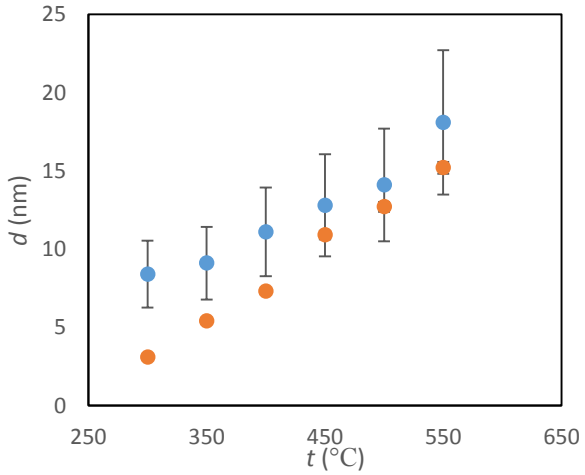

Figure 4.5: Dependence of the particle size obtained from Sherrer equation (orange) and from TEM analysis (blue) on the annealing temperature.

4.3 DNS measurements

In **Figure 4.6** are presented all separated contributions (spin incoherent, nuclear coherent and magnetic scattering) of prepared samples measured at temperature of 3 K. We can see, that separation was successful, which is confirmed by almost constant spin incoherent scattering. The nuclear coherent scattering of samples has similar trend as was obtained from PXRD analysis. There is a presence of Bragg's maxima from spinel structure of the sample and Bragg's maximum from used aluminium sample holder (at 2.6 $Å^{-1}$). Looking closely on magnetic scattering contribution, it can be seen the presence of magnetic reflection which are at the same position as Bragg's maxima of spinel structure. These reflections are from collinear magnetic structure (ferrimagnetic ordering). Moreover, there are additional magnetic reflections, which are not arising from the nuclear structure position, so called magnetic satellites. These magnetic satellites directly confirm the presence of spiral magnetic ordering of $CoCr_2O_4$ nanoparticles.

From the incoherent scattering contribution, **Figure 4.6**, we can see that the intensity of the incoherent scattering decreases with increasing annealing temperature, due to the decomposition of organic substances rich on hydrogen.

By comparing the magnetic dependence of magnetic scattering contributions (**Figure 4.7**), it can be obtained an information on magnetic phase transitions. The first is the blocking temperature of nanoparticles which corresponds to the appearance of collinear magnetic reflections. The second magnetic transition is with the arising of the magnetic satellites from non-collinear structure corresponding to the transverse conical magnetic structure. We can follow, that magnetic transitions changes with decreasing of particle size. From **Figure 4.8** it can be seen the trend of blocking and transition temperature with particle size. The values of blocking temperature shift towards lower temperature similar to the trend of blocking temperature for cobalt ferrite nanoparticles.[32].

From **Figure 4.9** of comparison of magnetic scattering of all prepared samples recorder at 3 K. It can be seen that the propagation vector changes with temperature, visible as the change of the position of magnetic satellites reflections. Looking closer at magnetic scattering with decreasing of nanoparticle diameter magnetic satellites gets more diffused.

That can be explained by the fact, that with decreasing nanoparticle diameter, the coherence length of spiral magnetic structure is close to the size value and therefore it gets diffusive character. This mean in real space that the period of spiral structure increases with decreasing size up to the critical size when the spiral magnetic order cannot exist due to similar size as coherence length of non-collinear structure. The critical size of nanoparticles is taken to be for AA350 sample, where in AA400 sample there is still significant magnetic satellite reflection while in AA350 sample are very diffused character. The critical size of the nanoparticles was determined on 9,1 nm (5.1 nm of coherent domain size) where the spiral structure can still exist. In smaller particles, the propagation vector is smaller (bigger period of spiral) than the dimensions of the particle and hence spiral magnetic structure cannot occur. Moreover, it can be seen that very broad fundamental reflections are present. The AA300 sample can be taken as the critical sample, where magnetic ordering can still exist. With further decrease of nanoparticle size it is expected to have not any magnetic order as was found in previous research[33] caused by collapsing long-range magnetic order.

The lattice parameter, obtained from the nuclear coherent scattering contribution, increases with particle size with slow approach to the bulk value, as it is expected for nanoparticles, **Figure 4.10**.

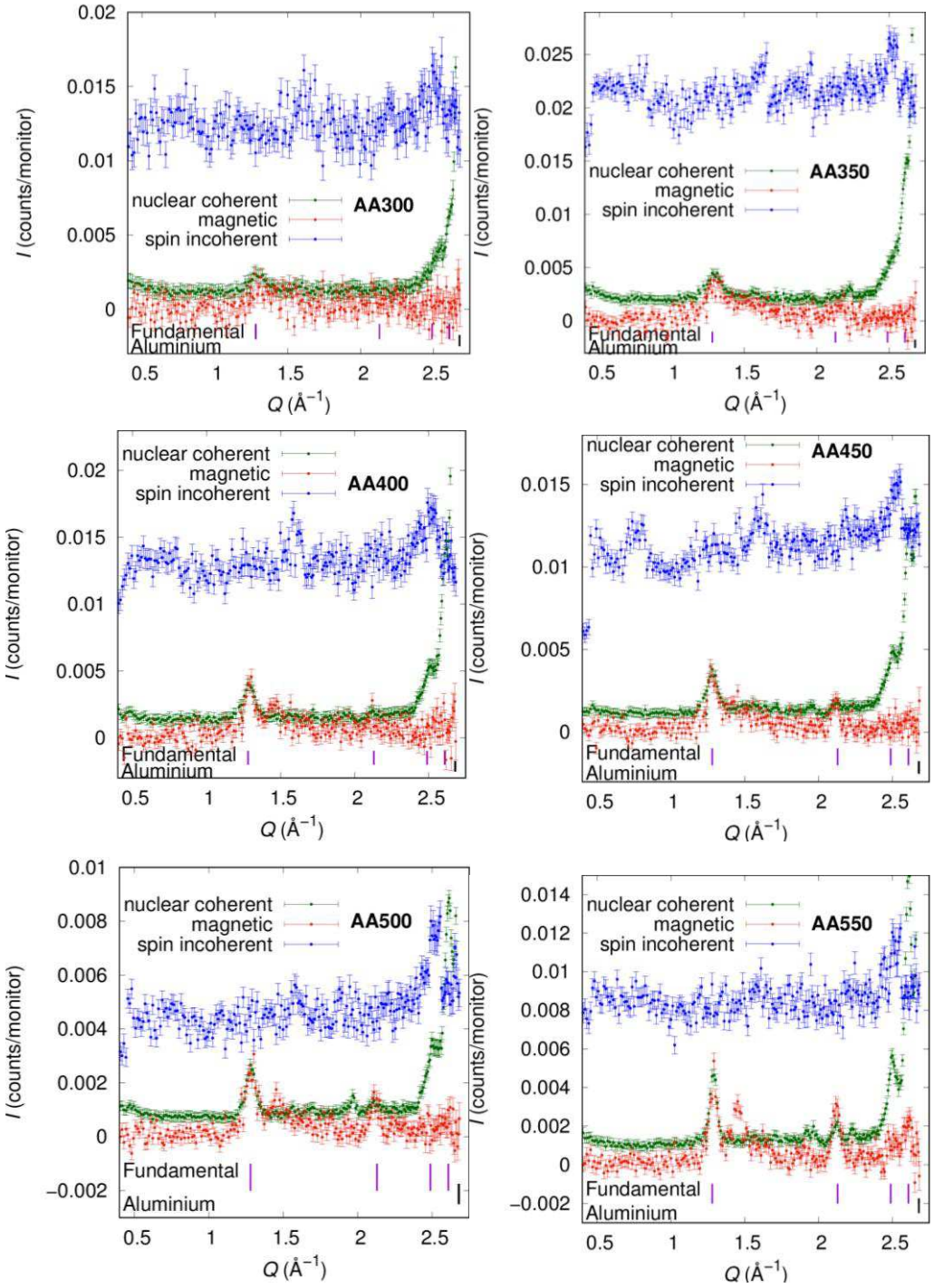

Figure 4.6: All separated scattering contributions of all cobalt chromite samples recorded at 3.2 K. Where the violet vertical lines represent the position of fundamental reflection and the black vertical line corresponds to Bragg's maximum of the aluminium.

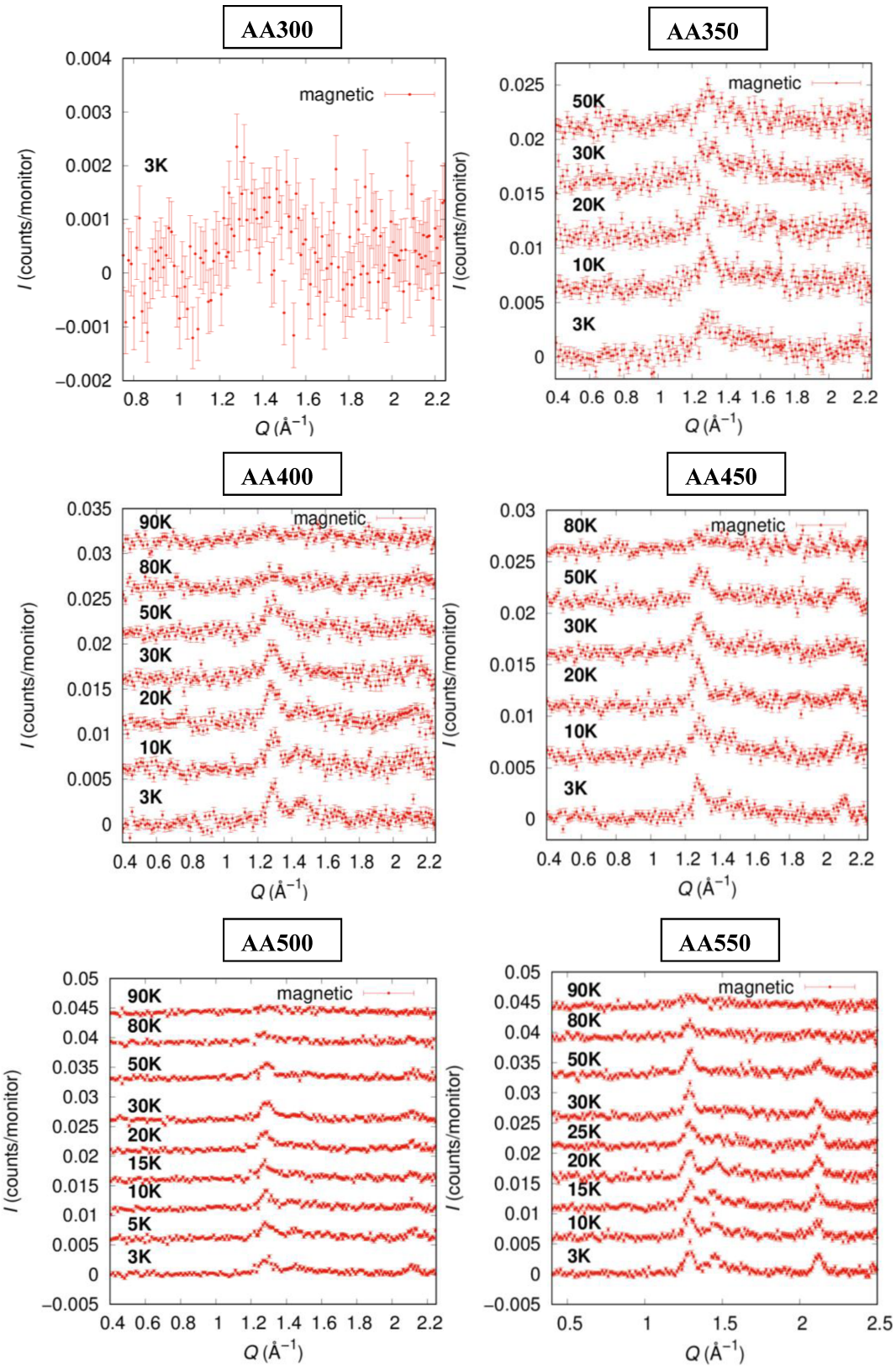

Figure 4.7: Temperature dependence of magnetic scattering of prepared samples. The sample AA300 was measured only at 3 K, where already at this temperature the fundamental reflections are very broad.

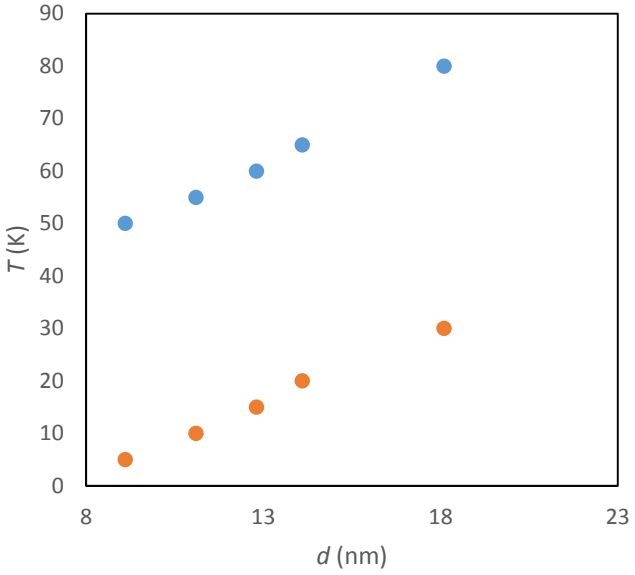

Figure 4.8: Dependence of the blocking temperature (blue) and the temperature of spiral transition (orange) on particle size.

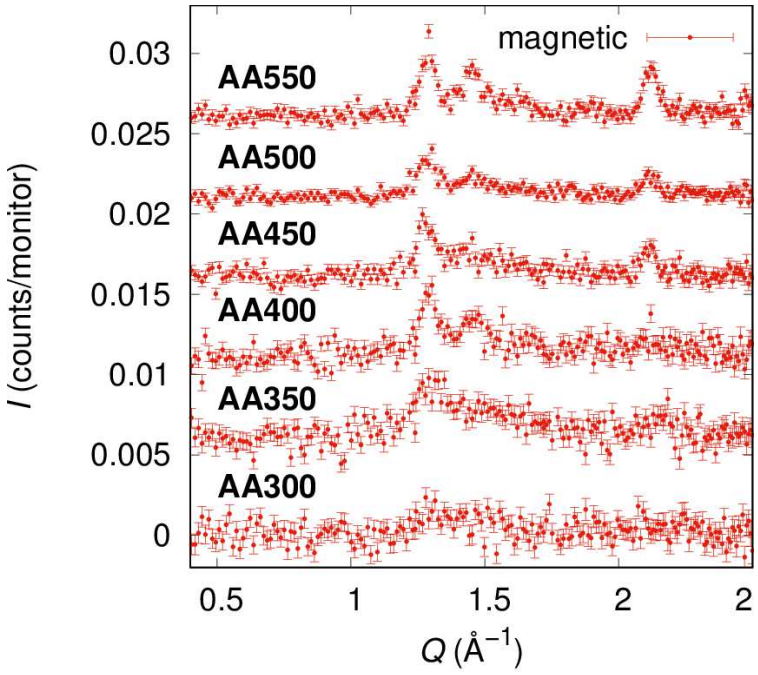

Figure 4.9: The comparison of magnetic scattering contributions of all samples recorded at 3 K.

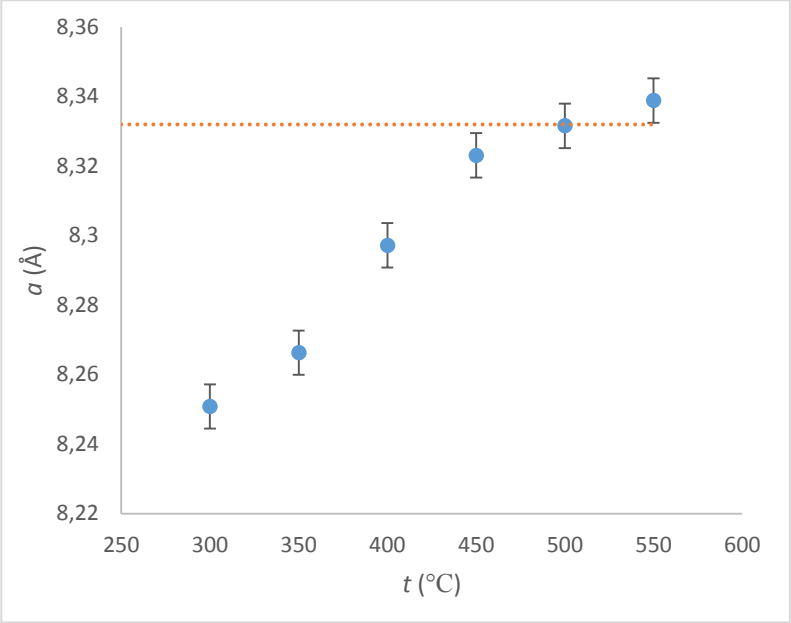

Figure 4.10: Dependence of the lattice parameter on the annealing temperature. The orange dotted line is the bulk value (8.3320 Å)[34].

5 CONCLUSIONS

Nanoparticles of $CoCr_2O_4$ with the particle diameter of 3.1 to 15.2 nm were synthetized using hydrothermal technique followed by annealing at 250 °C, 300 °C, 350 °C, 400 °C, 450 °C, 500 °C and at 550 °C for 2 hours. The phase composition and the spinel structure of $CoCr_2O_4$ was confirmed by PXRD experiments where the typical peaks of the spinel structure were presented.

From TEM analysis of micrographs we obtained the nearly spherical morphology of our prepared nanoparticles. Moreover, the distribution of particle sizes were obtained from TEM micrographs. The sizes determined by TEM are larger than the sizes determined by PXRD, which is in good agreement with the expected behavior.

The magnetic properties were evaluated at microlevel by means of neutron diffraction experiments with XYZ polarization analysis. All scattering contribution were successfully separated, which was indicated by nearly constant spin incoherent scattering contribution. The intensity of incoherent scattering contribution reflects the amount of hydrogen atoms, which are presented at surface of nanoparticles. The nuclear structure of material refined from nuclear coherent scattering were in good general agreement with PXRD experiments. From pure magnetic scattering cross section, we obtained all the magnetic phase transitions and we directly prove the existence of non-collinear structure in nanoparticles, which can be seen from appearance of the magnetic satellites in magnetic scattering contribution. Furthermore, the position of magnetic satellites slightly changes with the temperature, which indicates that the propagation vector (period) of the spiral also changes with temperature. Moreover, we have also found the critical particle size for creation of spiral structure.

The critical value of particle diameter of 9.1 nm. (coherent size of 5.1 nm) where the spiral magnetic ordering can still exist but with diffuse character as the period of spiral approaches the coherent size of nanoparticles. We have also found, that with next decrease of nanoparticle size (4.1 nm of coherent domain size), the non-collinear ordering can not exist and the fundamental reflections of long-range magnetic ordering
were broad, which with the next decreases of size leads to the collapsing of this magnetic order.

6 REFERENCES

[1] YAMASAKI, Y. *et al*. (2006): *Phys. Rev. Lett.*, **96**, 207204.

[2] CHANG, L. J. *et al*. (2009): *J Phys Condens Matter*, **21**, 456008.

[3] TOMIYASU, K. et. al. (2004): *Phys Rev B*, **70**, 214434.

[4] FIEBIG, M. (2005): J. Phys. D Appl. Phys. **38**, R123.

[5] FINO, D. *et. al*. (2008): *Powder Technol*. **180**, 74–78.

[6] FINO, D. *et. al*. (2007): *Top. Catal.* 42–43, 449–454.

[7] TOKURA, Y., MAGN J. (2007): *Magn. Mater*. **310**, 1145.

[8] SHUIJIN, L. *et al*. (2013): *Cryst Eng Comm*, **16**, 227-286.

[9] VESTAL, C. R., ZHANG Z. J. (2002): *Chem Mater*, **14**, 3817-3822.

[10] LAWES, G. *et al*. (2006): *Phys Rev B,* **74**, 024413.

[11] TOMIYASU, K., KAMAZAWA, K. (2006): *Physica B*, **392**, 16-19

[12] KITTEL, CH. (2005): Introduction to solid state physics, s. 417, ISBN 0-471-41526-X, 680 s.

[13] https://magwiki.wikispaces.com/Magnetic+Ordering

[14] http://www.physics.iisc.ernet.in/~aveek_bid/PH208/Lecture%2010%20Magnetism.pdf

[15] SCHMID, H. (1994): *Ferroelectrics*, 162, 317.

[16] KHOMSKII, D. K. (2009): *Physics*, **2**, 20.

[17] TOKURA, Y. et al. (2014): *Journal of Magnetism and Magnetic* Materials, **310**, 1145-1150.

[18] DEMOKRITOV, S.: https://www.uni-muenster.de/Physik.AP/Demokritov/en/Forschen/Forschungsschwerpunkte/mBECwam.html

[19] LEFMANN, K. et al. (2007): Neutron Scattering: Theory, Instrumentation, and Simulation, s. 9, s. 15-16, s. 24-26, Technical University of Denmark, 244 s.

[20] PYNN, R. (1990): Neutron scattering A PRIMER, Los Alamos Neutron Science Center, s. 3, 27 s.

[21] BRÜCKEL, T. et al. (2012): Neutron Scattering Neutron Scattering Lectures of the JCNS Laborator Course held at Forschungszentrum Jülich and the research reactor FRM II of TU Munich In cooperation with RWTH Aachen and University of Münster, kap.4 s. 12, kap.4 s. 13, kap.7 s. 3, kap.7 s. 4, kap.7 s. 6, kap.7 s. 7, ISBN 978-3-89336-789-4.

[22] BRÜCKEL, T. et al. (2012): Neutron Scattering Experiment Manuals of the JCNS Laborator Course held at Forschungszentrum Jülich and the research reactor FRM II of TU Munich In cooperation with RWTH Aachen and University of Münster, DNS 3, ISBN 978-3-89336-790-0.

[23] DUTCH, S.: Natural and Applied Sciences, University of Wisconsin-Green Bay.

[24] https://chem.libretexts.org/Textbook_Maps/Inorganic_Chemistry_Textbook_Map/Map%3A_Inorganic_Chemistry_(Wikibook)/Chapter_08%3A_Ionic_and_Covalent_Solids_-_Structures/8.6%3A_Spinel%2C_perovskite%2C_and_rutile_structures, (2015)

[25] MOMMA, K., IZUMI, F. (2011): J. Appl. Cryst., **44**, 1272-1276.

[26] BYRAPPA, K. et al. (2001): Handbook of Hydrothermal Technology, a Technology for Crystal Growth and Material Processing, 7, 863 s. ISBN 0-8155-1445-X, University of Mysore Manasagangotri Mysore, India.

[27] RABENAU, A. (1985): *Angew. Chem.*, **24**, 1026-1040.

[28] EANES, M. (2000): Synthesis and Characterization of Alkali Silver Chalcogenides and Alkali Rare Earth Germanates by Supercritical Fluids, Clemson University.

[29] CHIEN, A.T. (1998): Hydrothermal Epitaxy of Peroksite Thin Films.

[30] C. A. Schneider, W. S. Rasband and K. W. Eliceiri, *Nat Meth*, 2012, **9**, 671-675.

[31] A. L. Patterson, *Physical Review*, 1939, **56**, 978-982.

[32] VEJPAROVÁ, J.P. *et al.* (2005): *Superparamagnetism of Co-Ferrite Nanoparticles*

[33] ZÁKUTNÁ, D. *et al.* (2016): *RSC Adv.*, **6**, 107659.

[34] Crystallographic and Crystallochemical Database for Minerals and their Structural Analogues, Institute of Experimental Mineralogy, Russian Academy of Sciences.